

# Promoting the OH<sup>-</sup> Ion Conductivity of Chitosan Membrane Using Quaternary Phosphonium Polymer Brush Functionalized Graphene Oxide

Lei Liu<sup>\*</sup>, Guoping Sun

School of Materials and Chemical Engineering, Zhongyuan University of Technology, Zhengzhou 450007, China

\*E-mail: [liscientific@126.com](mailto:liscientific@126.com)

Received: 9 June 2017 / Accepted: 2 August 2017 / Published: 12 September 2017

---

Herein, graphene oxide functionalized with polymer brushes containing quaternary phosphonium (QPGO) was synthesized using the atom transfer radical polymerization (ATRP) technique and then incorporated into chitosan (CS) matrix to prepare composite membrane. Numerical simulation and computation results revealed that the electrostatic potential of the selected QP group was much lower than the commonly used quaternary ammonium (QA) group, hinting a better OH<sup>-</sup> dissociation and conduction ability. The brush-like structure afforded QPGO densely distributed QP groups with high mobility and activity. The incorporation of QPGO conferred composite membranes with hierarchical structures, where long-range pathways with locally enriched carrier sites were constructed in polymer-filler interfaces. The unique architecture significantly promoted hydroxide conductivity. Particularly, composite membrane containing 1.5 wt% QPGO acquired a 220% augment in conductivity at 20 °C under saturated humidity. Based on this benefit, QPGO-filled membranes displayed much higher fuel cell performances than that of CS control and GO-filled membranes, and the maximum energy output reached approximately 110 mW/cm<sup>2</sup>.

---

**Keywords:** quaternary phosphonium functionalized graphene oxide; polymer brush; electrostatic potential energy; composite membrane; hydroxide ion conductivity

## 1. INTRODUCTION

Alkaline fuel cell (AFC) has gained growing attention due to the numerous advantages in terms of low fuel permeation as well as enhanced reaction kinetics, and thus the accessibility of using non-noble materials (such as Ni and Co). [1-3] As the hard core part of AFC, alkaline anion exchange membrane (AEM) should efficiently conduct OH<sup>-</sup> ions to fulfil the energy conversation and

simultaneously serve as a barrier between fuel and oxidant. The hydroxide conductivity directly determines the fuel cell performances, including open-circuit voltage (OCV) and energy output. [4,5] However, the conductivities of AEMs are always unsatisfactory when compared to their acidic counterparts (proton exchange membrane) due to the intrinsic low mobility of  $\text{OH}^-$  associated with the weak basicity of the cation site. [6] Consequently, there is in great demand to design and prepare AEMs with high hydroxide ion conductivity.

To circumvent this issue, plenty of polymers functionalized with various cationic groups such as quaternary ammoniums, [7] imidazoliums, [8,9] phosphoniums, [10] and guanidinium [11] have been developed. Generally, the loading amount of charged groups determines the hydroxide ion conductivity, that is, a high hydroxide ion conductivity can be obtained through the increase of charged groups in the membrane. However, this high conductivity is always accompanied by excessive water uptake, leading to the deterioration of mechanical integrity, which is another fundamental requirement for AEMs. [12,13] A promising solution to this problem is developing polymers with deliberately designed architectures, for example, block and comb-shaped copolymers. The notable incompatibility between polymer backbones and ionic side chains associated with enthalpy can drive it to self-assemble into highly ordered phase-separated morphology composed of continuous hydrophobic backbone and interconnected ion transfer channels, accounting for mechanical integrity and hydroxide conduction, respectively. [14-16] Watanabe et al. prepared aromatic multiblock copoly(arylene ether)s with clustered ionic groups in the hydrophilic blocks. The exclusive polymer architecture results in nanophase separation between the conducting and nonconducting phases, and bestows higher hydroxide conductivities compared with their random copolymer counterparts without sacrificing mechanical stability. [17] Li and co-workers have prepared comb-shaped poly (2,6-dimethyl-1,4-phenylene oxide)s with quaternary ammonium groups attached by long alkyl side chains. The obtained membrane displays a comparable conductivity with conventional ones at a much lower water uptake. [18] Although these polymers exhibit unprecedented conduction ability and acceptable mechanical property, the preparation process is always complicated and difficult to manipulate precisely. [15]

Apart from developing polymers with unique architectures, another approach for preparing membranes with sufficient ion conductivity and mechanical properties is organic-inorganic hybridization. [19,20] The incorporation of inorganic fillers (especially for functionalized 1-D and 2-D ones), on one hand, can construct substantial long-range transfer channels along the interfaces, serving as short-cuts for ion conduction; on the other hand, the inherent mechanical strength of inorganic filler can prohibit the dimensional deterioration of composite membrane to some extent. Li and co-workers incorporated ionic liquid functionalized carbon nanotubes (ILNTs) into poly (2,6-dimethyl-1,4-phenylene oxide) to prepare composite membrane. The addition of 0.3% ILNTs can elevate the conductivity of membranes from 0.0129 to 0.0252  $\text{S cm}^{-1}$ . [21] In addition to the structure, the loading amount and the conduction capability of carrier sites within the channel is another critical factor for hydroxide ion conductivity. Researchers have incorporated halloysite nanotubes and functionalized halloysite nanotubes into polymer to prepare composite membranes, and have found that composite membranes with functionalized halloysite nanotubes exhibit 2.4-time enhancement of conductivity compared to ones with unmodified halloysite nanotubes. [22] For enhancing the conduction ability of inorganic material based interfacial channel, there are generally two methods: coating polymer layer

and grafting polymer brushes. Compared with polymer layer, the brush-like structure possesses more advantages in terms of better chain mobility, larger contact area with polymer matrix, and more available carrier sites. [23]

Herein, novel composite AEMs were prepared by embedding quaternary phosphonium contained polymer brush functionalized GO (QPGO) into chitosan (CS) matrix. CS was chosen as the membrane matrix owing to its good film forming and mechanical properties as well as low cost.[24,25] Graphene oxide (GO), with large surface area, high aspect ratio, and abundant oxygen-containing groups (easily modified), has been extensively utilized in a variety of research fields. [26,27] The GO was then functionalized with polymer brushes containing appreciable number of quaternary phosphonium groups, which have been demonstrated to be very strong base and display high  $\text{OH}^-$  conduction capability. [28] The microstructures and physicochemical properties of membranes were investigated in detail. Meanwhile, the hydroxide ion conductivity and transfer mechanism were evaluated.

## 2. EXPERIMENTAL

### 2.1. Materials and Chemicals

Natural graphite powders (45 mm) were purchased from Sigma-Aldrich. Chitosan (CS) with the degree of deacetylation of 95% was provided by Golden-Shell Biochemical Co. (Zhejiang, China). Allyltriphenylphosphonium bromide (APB), triethylamine (TEA), 2,2-bipyridine (BPy), and Copper (II) bromide ( $\text{CuBr}_2$ ) were purchased from Alfa Aesar and used as received. Acetonitrile, potassium hydroxide (KOH, 99.9%), acetic acid,  $\text{KMnO}_4$ , concentrated sulfuric acid, phosphoric acid, and anhydrous alcohol were available from Tianjin Kermel Chemical Reagent Co., Ltd.  $\text{H}_2\text{O}_2$  was supplied by Fengchuan Chemical Reagent Co., Ltd. 2, 2-Azobisisobutyronitrile (AIBN) and hydrochloric acid (HCl, 37%) were purchased from Kewei Chemistry Co., Ltd. De-ionized water (18  $\text{M}\Omega/\text{cm}$ ) was used throughout the experiment.

### 2.2. Synthesis of quaternary phosphonium functionalized GO (QPGO)

Graphene oxide (GO) nanosheets were synthesized by oxidizing natural graphite powders according to the improved Hummer's method. [29] The synthesis of QPGO was based on atom transfer radical polymerization (ATRP) technology. [30] The detailed synthetic procedure was described as follows. GO (0.5 g) was dispersed in THF (50 mL) in round-bottom flask (100 mL) with sonication in ice bath for 0.5 h. Then, TEA (6 mL) and BIBB (5 mL) were added into the solution dropwise and stirred for 2 h. Afterwards, the reaction system was sealed to insulate ambient water vapors and kept at 35 °C with magnetic agitation for 24 h. Subsequently, the modified GO (GO-Br) was collected by centrifugation and washed with anhydrous alcohol and followed by drying in vacuum oven.

GO-Br (1.0 g),  $\text{CuBr}_2$  (0.058 g, 0.188 mmol), BPy (0.058, 0.38 mmol), APB (6.47 g, 16.88 mmol) and methanol (40 mL) were dispersed in a Schlenk flask (100 mL) with ultrasonic treatment to form a homogenous solution. Then ABIN methanol solution (0.028 mmol  $\text{mL}^{-1}$ ) was added to the

mixture. Immediately, the reaction system was airtight with an oil-sealed device and was kept under flowing  $N_2$  to vent the air. The system was refluxed at  $75\text{ }^\circ\text{C}$  for 24 h. Finally, the resultant product (named QPGO) was obtained by centrifugation, washing with anhydrous alcohol and then dried in vacuum oven.

### 2.3. Preparation of the Membranes

CS (1.2 g) and 0-2.5 wt % QPGO or GO were added into acetic acid (2 wt %, 60 mL) solution at  $80\text{ }^\circ\text{C}$  with mechanical agitation to produce a homogeneous solution. Then, the solution was cooled down to  $25\text{ }^\circ\text{C}$ , and glutaraldehyde (GA, 2%, v/v) aqueous solution (5 mL) was added dropwise. The mixture was stirred vigorously at  $25\text{ }^\circ\text{C}$  for 3 h. Subsequently, the resulting solution was cast onto a glass plate until the solvent evaporated completely at  $25\text{ }^\circ\text{C}$ . Afterward, all of the membranes were immersed in  $0.5\text{ mol L}^{-1}$  KOH solution for 24 h to obtain the  $\text{OH}^-$  form membrane. Finally, the membranes were washed thoroughly with deionized water to remove the residual KOH and kept in sealed bag before testing to avoid accessing to  $\text{CO}_2$ . The obtained membranes were labelled as CS, CS/GO- $X$ , and CS/QPGO- $X$ , respectively, where  $X$  ( $X = 0.5, 1.5, 2.5$ ) represented the weight percentage of filler to the CS matrix.

### 2.4. Characterization of the GO, QPGO, and Membranes

Transmission electron microscopy (TEM, Tecnai G2 20 S-TWIN) was used to observe the morphologies of GO and QPGO at an acceleration voltage of 100 kV. The sample was prepared by dripping the dilute GO or QPGO dispersion onto the carboncoated copper grids and dried in vacuum oven. FTIR measurements were conducted on a Nicolet (MAGNA-IR 560) to characterize the chemical structure of the GO, QPGO, and membranes ( $1.5\text{ cm} \times 1.5\text{ cm}$ ) in the wave length range from  $4000$  to  $500\text{ cm}^{-1}$  at room temperature. Cross-section morphologies of membranes were observed on a scanning electron microscope (SEM, Nanosem430). The membrane samples were freeze-fractured in liquid nitrogen and then sputtered with platinum prior to measurements. The thermal stabilities of the nanosheets and membranes were investigated using a TGA-50SHIMADZU in the temperature range of  $30$ – $800\text{ }^\circ\text{C}$  at a ramp rate of  $10\text{ }^\circ\text{C min}^{-1}$  under  $N_2$  atmosphere. Mechanical property of the membrane ( $1.0\text{ cm} \times 4.0\text{ cm}$ ) was tested using Instron mechanical tester (Testometric 350 AX) with the elongation rate of  $5.0\text{ mm min}^{-1}$  at room temperature. The crystalline structures of the nanosheets and membranes were performed by X-ray diffraction (XRD) in the range of  $5^\circ$ – $60^\circ$ .

### 2.5. Determination of the Ion Exchange Capacity (IEC) Values, Water Uptake, and Swelling Ratio

The ion exchange capacity (IEC) values of the nanosheets and membranes were determined by traditional Mohr titrations. The dry sample (0.4 g) was soaked in an HCl solution ( $0.1\text{ mol L}^{-1}$ , 20 mL) for 24 h. Subsequently, the solution was titrated with standard KOH solution ( $0.1\text{ mol L}^{-1}$ ) using phenolphthalein as indicator. The IEC values were calculated by equation (1):

$$IEC(\text{mmol g}^{-1}) = \frac{(M_{1,\text{HCl}} - M_{2,\text{HCl}})}{W_{\text{dry}}} \quad (1)$$

where,  $M_{1,\text{HCl}}$  and  $M_{2,\text{HCl}}$  were the molar of HCl before and after equilibrium, respectively.  $W_{\text{dry}}$  was the weight of the dried membranes.

Water uptake and swelling ratio of the membranes were measured to evaluate the water absorbing capability and structural performance by monitoring the change of weight and area between the wet and dry membranes. Prior to the measurement, the samples were dried at 80 °C in vacuum until a constant weight was obtained. Then, the membranes were soaked in temperature-controlled deionized water for more than 48 h, and immediately measured to determine the weight and the area of wet membrane after removing the surface water with absorbent paper. The water uptake and swelling ratio of the membranes were calculated by equation (2) and (3), respectively.

$$\text{Water uptake (\%)} = \frac{(W_{\text{wet}} - W_{\text{dry}})}{W_{\text{dry}}} \times 100 \quad (2)$$

$$\text{Swelling ratio (\%)} = \frac{(A_{\text{wet}} - A_{\text{dry}})}{A_{\text{dry}}} \times 100 \quad (3)$$

where  $W_{\text{wet}}$  (g) and  $A_{\text{wet}}$  (cm<sup>2</sup>) were the mass and area of the wet sample, respectively.  $W_{\text{dry}}$  (g) and  $A_{\text{dry}}$  (cm<sup>2</sup>) were the corresponding values in a dry state.

## 2.6. Hydroxide Ion Conductivity

The hydroxide ion conductivity of the membrane was measured by two-probe AC impedance spectroscopy. The amplitude of the sinusoidal signal for AC impedance was set as 20 mV rms over a frequency range of 1 MHz to 100 Hz. The hydroxide ion conductivities of membranes were tested under both anhydrous (0% RH) and saturated humidity (100% RH) using constant temperature and humidity cases. The hydroxide ion conductivity of the membrane was calculated according to equation (4):

$$\sigma = \frac{l}{R \times A} \quad (4)$$

where  $l$  (cm),  $A$  (cm<sup>2</sup>), and  $R$  (Ω) represented the sample thickness, effective contact area, and resistance, respectively.

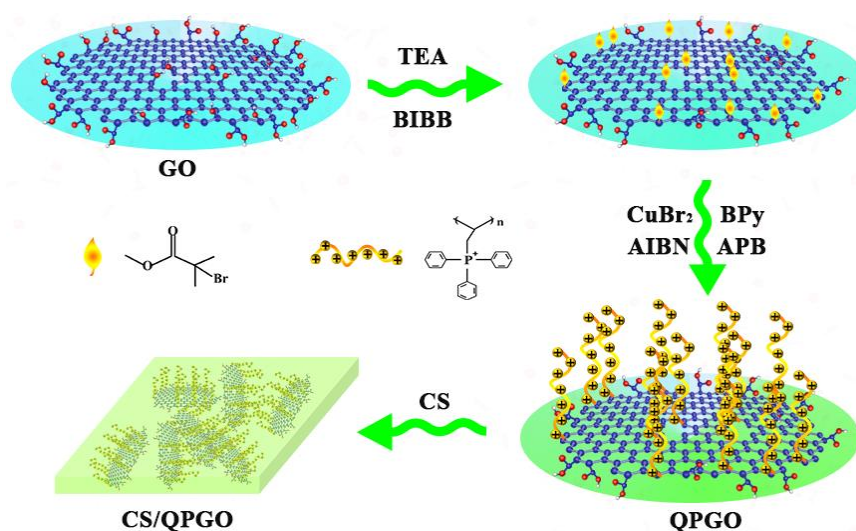
## 2.7. Fuel Cell Performance

The obtained membranes were assembled into membrane electrode assembly (MEA) to evaluate the practical performance in fuel cell. Specifically, Pt/C catalyst with Pt loading of 10 mg cm<sup>-2</sup> was used for both the anode and the cathode. The MEA was fabricated by hot-pressing the membrane with catalytic electrode at a pressure of 4 MPa at 60 °C for 3 min. The single cell testing was performed at 60 °C and 100% RH under atmospheric pressure. During the testing, the anode was fed with a 5.0 M ethanol solution at a flow rate of 1.0 mL min<sup>-1</sup>, and the cathode was fed with air at a flow rate of 400 mL min<sup>-1</sup>.

### 3. RESULTS AND DISCUSSION

#### 3.1. Characterizations of GO and QPGO

The preparation process of QPGO was illustrated in Scheme 1, containing two steps: the introduction of initiators on GO surface and the grafting of QP cations-containing polymer brushes along the vertical axis direction of the GO sheets. The as-prepared GO and QPGO were firstly investigated by TEM, FTIR, and XRD (Fig. 1). TEM image (Fig. 1a) revealed that GO sheet was transparent with some wrinkles due to the  $\pi$ - $\pi$  interactions between the basal planes of GO [31]. Upon functionalization with polymer brushes, the transparency of QPGO (Fig. 1b) decreased slightly. The lateral size of both GO and QPGO were found to fall in the 3-5  $\mu\text{m}$  range, favoring of constructing long-ranged pathway in the composite membrane. The chemical structures of GO and QPGO were characterized by FTIR (Fig. 1c).



**Scheme 1.** Synthesis process of QPGO and composite membranes.

The absorption peaks at 1621, 1220, and 1043  $\text{cm}^{-1}$  were attributed to the aromatic domain (C=C), C-O bond stretching vibration, and asymmetric stretching vibration of epoxy bond, respectively. [32] Grafting quaternary phosphonium contained polymer brushes afforded QPGO a new characteristic peak at approximately 1108  $\text{cm}^{-1}$  and a strong broad band at 1520–1283  $\text{cm}^{-1}$ , assigned to phosphonium groups and benzene rings, respectively. [33] The XRD patterns of GO and QPGO were shown in Fig. 1d. It was observed that GO exhibited a typical diffraction band at approximately  $2\theta=9.4^\circ$ , corresponding to the basal spacing of 0.89 nm, which was larger than that of graphite ( $0.33\text{ nm}$ ,  $2\theta=27^\circ$ ). The presence of oxygen containing groups (i.e., hydroxyl, carboxylic and epoxide) at the edges and on the basal planes of GO should be responsible for this increase of interlayer distance. Upon functionalization, QPGO displayed a typical diffraction band at approximately  $2\theta=9.7^\circ$ , corresponding to the basal spacing of 0.88 nm, which was comparable to the pristine GO. This phenomenon indicated that GO retained its structural integrity during the preparation process. For

functionalized nanofiller, the distribution of conductive sites was important for hydroxide conduction. The distribution of quaternary phosphonium groups on QPGO were probed by EDS elemental mapping. Fig. 1e illustrated a relatively homogeneous distribution of P species, indicating a homogeneous distribution of quaternary phosphonium contained polymer brushes on QPGO. It was interesting to find that, in TGA curves (Fig. 1f), QPGO presented lower weight losses (11.8%) than GO (14.8%) in the temperature range of 30–150 °C, which was generally a stage for water loss. Considering the long brushes with densely appended quaternary phosphonium groups, QPGO should possess stronger water absorbing capacity and thus exhibit higher weight losses than GO in this stage. Numerical simulation and computation results indicated that the dipole moment of QP was 0.2442 Debye, indicating an inferior hydrophilicity. This phenomenon was further verified by the decreased bond intensity of QPGO approximately 3380  $\text{cm}^{-1}$  for absorbed  $\text{H}_2\text{O}$  in FTIR spectra. At the second stage (180–380 °C), QPGO exhibited elevated thermo-stability compared to GO due to the coverage of polymer brushes, which delayed the decomposition of oxygen-containing functional groups of GO. Collectively, these results validated the successful grafting of quaternary phosphonium contained polymer brushes on GO nanosheets.

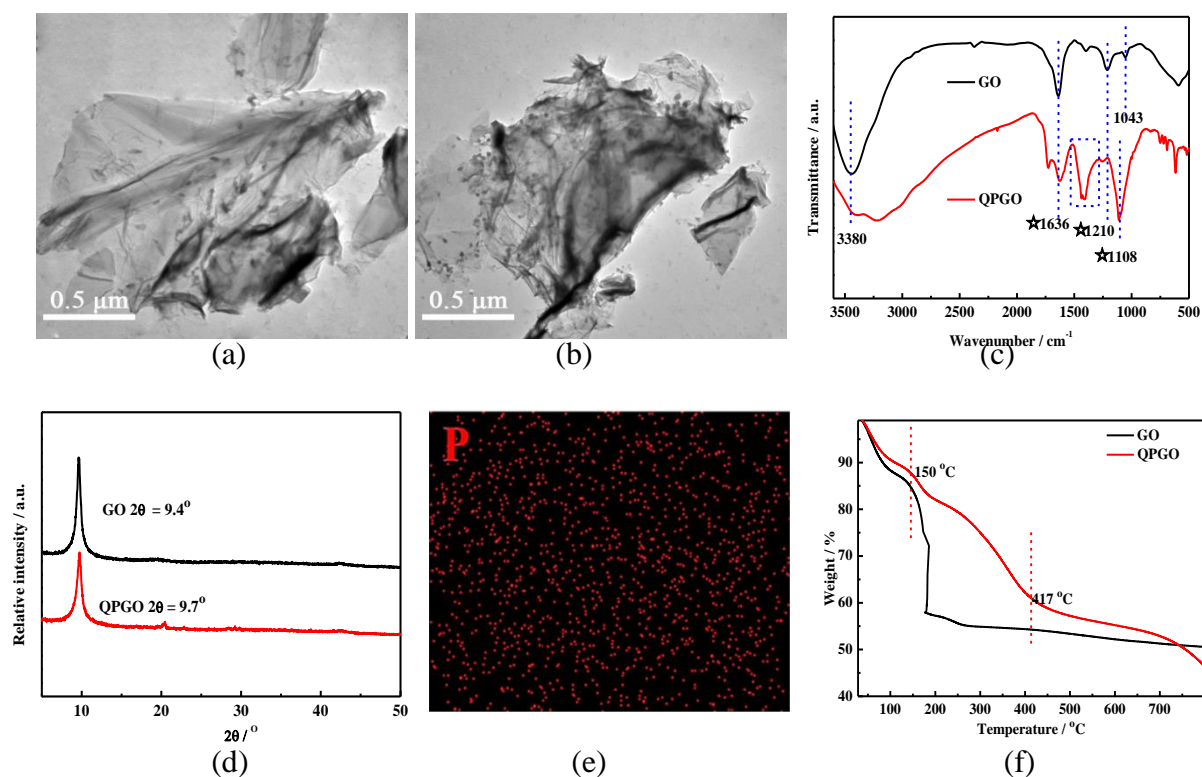


**Figure 1.** TEM images of GO (a) and QPGO (b); FTIR spectra (c), XRD patterns (d) of GO and QPGO; EDS elemental mappings of P in QPGO (e), TGA curves of GO and QPGO(f).

### 3.2. Characterizations of Membranes

The composite membranes were prepared *via* solution casting method. The cross-section morphologies of CS control and composite membranes were presented as Fig. 2a, b, and c. It was found that CS control membrane was homogeneous and dense, without cracks or pinholes. Upon the

incorporation of GO and QGPO, the cross-section of composite membranes displayed obvious wrinkles, portending notable interferences of fillers on stacking of CS chains through steric effect. Meanwhile, the nanosheets retained their pristine structure and were dispersed evenly throughout the whole cross-section. By comparison, the cross-section of CS/QPGO-1.5 was found to be rougher than that of CS/GO-1.5 due to the presence of polymer brushes, which strongly disturbed the stacking of CS chains.

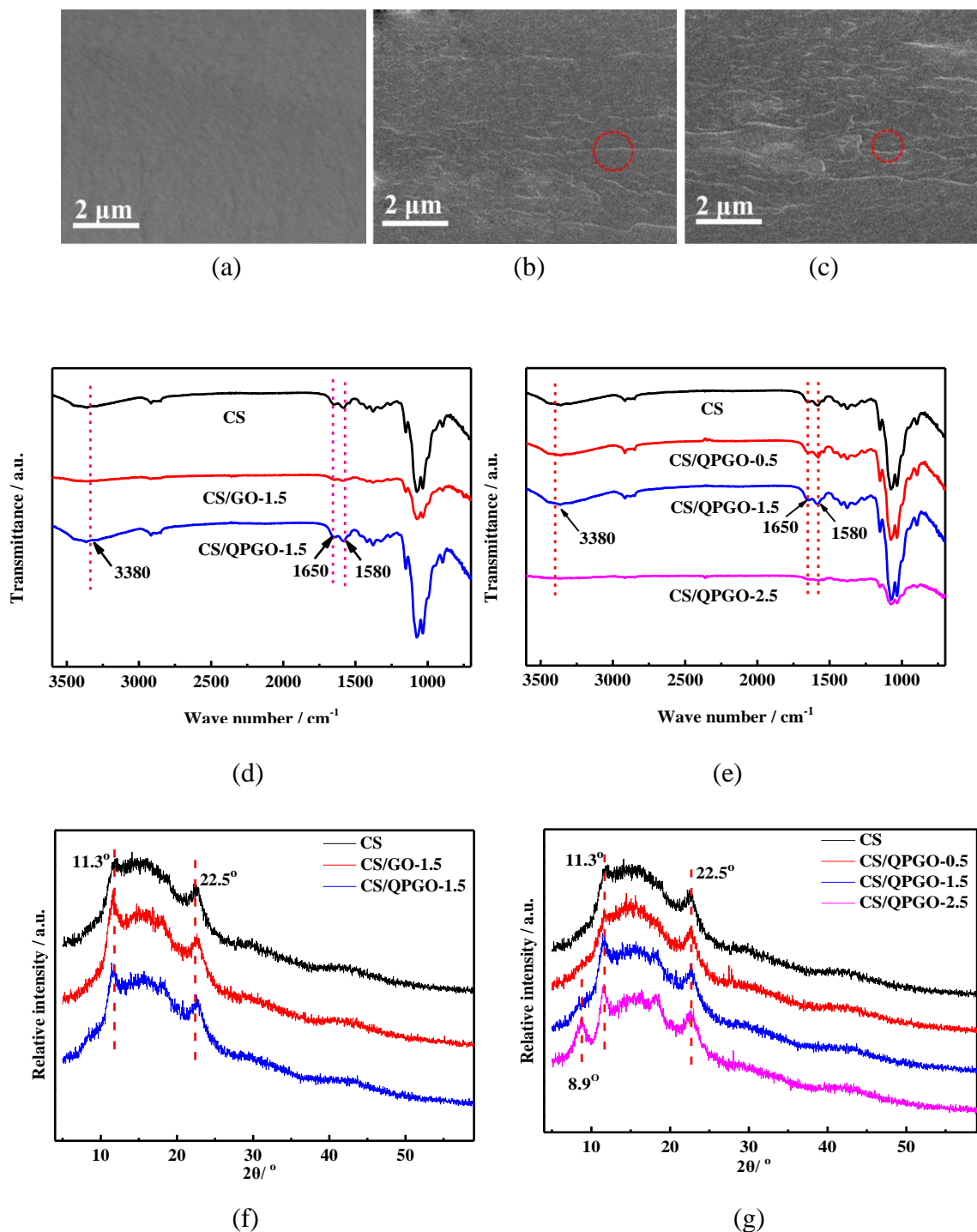


**Figure 2.** SEM images of CS control (a), CS/GO-1.5 (b), and CS/QPGO-1.5 (c); FTIR spectra of the membranes (d and e). XRD patterns of membranes (f and g).

The CS control and composite membranes were then subjected to FTIR characterization and the results were shown in Fig. 2d and e. All of the membranes displayed two characteristic peaks for CS matrix at 1650 (amide I), 1580 (amide II)  $\text{cm}^{-1}$ . [34] Compared with CS control membrane, CS/GO-1.5 displayed pronounced intensity decline for all these peaks. This should be ascribed to the presence of oxygen-containing groups on GO, which generated hydrogen bond interactions with functional groups on CS chains, and thus weakened the peak intensity. Interestingly, the incorporation of QPGO afforded CS/QPGO-1.5 enhanced intensity of characteristic bands compared with CS/GO-1.5. This phenomenon should be attributed to the weakened hydrogen bond interactions and thus increased amount of free functional groups associated with the decreased crystallinity, as testified by the promoted intensity of adsorbed water band near 3380  $\text{cm}^{-1}$  and XRD results in Fig. 2f and g. In XRD patterns, all the membranes exhibited characteristic bands of CS phase at  $2\theta=11.3^\circ$  and  $22.5^\circ$ , which mainly originated from the intermolecular hydrogen bond interactions.[35] Upon the incorporation of the nanosheets, the intensity of crystallization peaks decreased due to mutual spatial and interfacial interference from nanofillers. Generally, materials with distinct crystalline domains will have sharp diffraction peaks with high intensities in XRD patterns, whereas those peaks will be broadened for amorphous materials. This can be monitored with the value of the full width at half maximum (FWHM) of the peak. The crystallinity has an inverse relationship with the FWHM, in other words, the lower value of FWHM, the higher crystallinity is. [36] By comparison, the values of FWHM (as shown in Table 1) increased upon the addition of nanosheets, indicating a decreased crystallinity for composite membranes. Meanwhile, CS/GO-1.5 exhibited relatively lower value of FWHM, indicating a higher crystallinity for than that of CS/QPGO-1.5. This was presumably due to the outstretched polymer brushes, which interfered with the stacking of CS chains and thus decreased the crystallinity. Increasing the QPGO content would further reduce the crystallinity, while excessive amounts would lead to the restacking of nanosheets as verified by the appearance of characteristic peak of QPGO in CS/QPGO-2.5 (Fig. 2g). The crystalline properties of the membranes played important roles on ion conduction, and composite membranes with decreased crystallinity were anticipated to display enhanced ion conduction capability.

**Table 1.** The values of full width at half maximum (FWHM) for CS control, CS/GO-1.5, and CS/QPGO-X membranes.

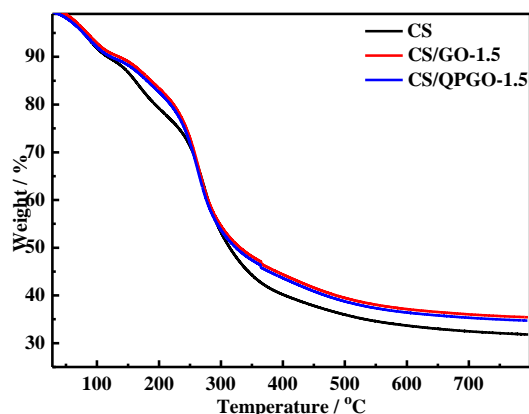
Sample	FWHM $^\circ(11.3^\circ)$	FWHM $^\circ(15.1^\circ)$	FWHM $^\circ(22.5^\circ)$
CS	2.0	8.3	2.4
CS/GO-1.5	2.1	8.4	2.5
CS/QPGO-0.5	2.2	8.5	2.6
CS/QPGO-1.5	2.3	8.9	2.8
CS/QPGO-2.5	2.4	9.0	2.9

The thermal properties of the membranes were characterized by TGA analysis, as shown in Fig. 3a and b. The CS control membrane underwent three degradation processes. The first stage (30–120  $^\circ\text{C}$ ) was attributed to the evaporation of absorbed water in membranes. The second stage (235–340  $^\circ\text{C}$ ) was ascribed to the degradation of attached functional groups in CS chains. The third stage was assigned to

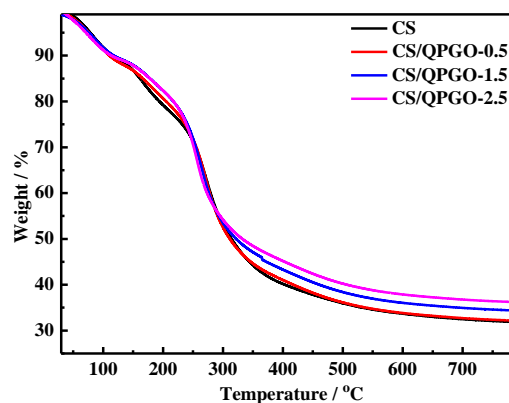
degradation of polymer backbones of CS (340–800 °C). By comparison, incorporating GO conferred CS/GO-1.5 decreased weight losses in the first and second stages, due to the presence of hydrogen bond interactions between oxygen-containing groups on GO and functional groups on the CS chains, which inhibited the water adsorption and the degradation of functional groups. Compared with CS/GO-1.5, CS/QPGO-1.5 displayed decreased weight losses in the first two stages. This phenomenon should be attributed to the weakened hydrogen bond interactions and decreased crystallinity, which generated increased amount of free hydrophilic functional groups and thus more absorbed water. It should be noted that CS/QPGO exhibited lower char yield than CS/GO, which was due to the degradation of long polymer brushes. The influence of filler content on thermal degradation behavior was shown in Fig. 3b. It could be seen that the thermostable QPGO conferred the composite membrane with promoted thermal stability as the filler content increase.

**Table 2.** IEC values, mechanical properties, hydroxide ion conductivities,  $E_a$ , and water uptake of the membranes in this work and literatures.

Membrane	IEC (mmol g <sup>-1</sup> )	Stress (MPa)	Temperature (°C)	$\sigma$ (mS/cm)	$E_a$ (kJ/mol)	Reference
CS/GA	--	38.0	RT	1.0	--	[37]
[PVMIm][OH] <sub>10</sub> - DVB <sub>4</sub>	0.21	50.2	30	0.16	15.5	[38]
GPPO-0.05	0.37	42.3	RT	11.0	--	[39]
QPVA/5 wt% GA	0.41	--	30	1.2	18.0	[40]
CS/QPGO-1.5	0.44	44.7	20	4.95	18.5	This study
PES-MeIm/OH	0.56	--	25	1.8	--	[41]
QPPO	0.70	--	30	4.3	--	[42]
FPAEO-1.0MIM	1.14		20	4.5	19.7	[43]
QPPO/SiO <sub>2</sub> - 2.8%	2.25	20.0	30	9.9	18.0	[44]



(a)



(b)

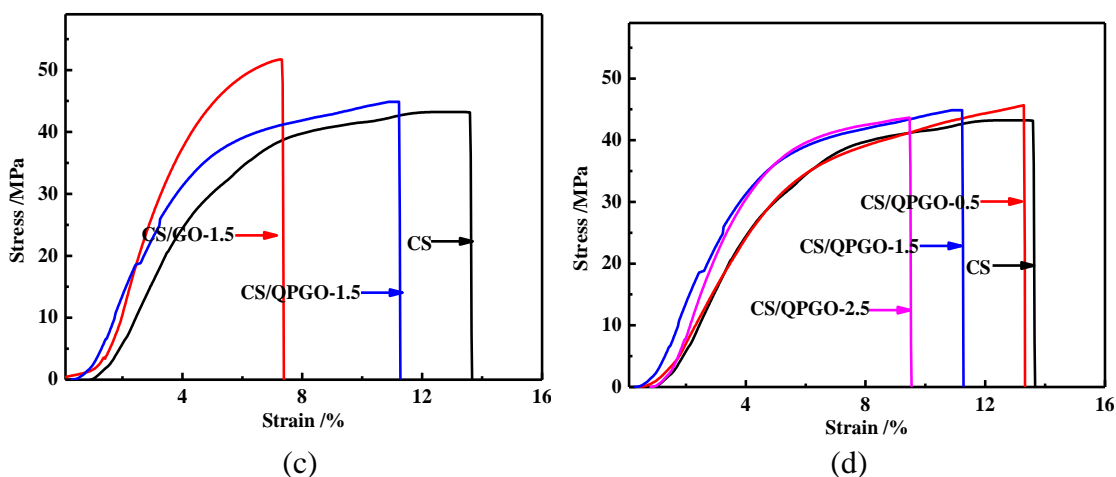


**Figure 3.** TGA curves (a and b) and stress-strain curves (c and d) of the membranes.

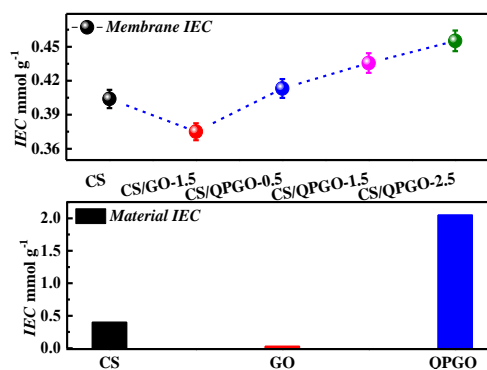
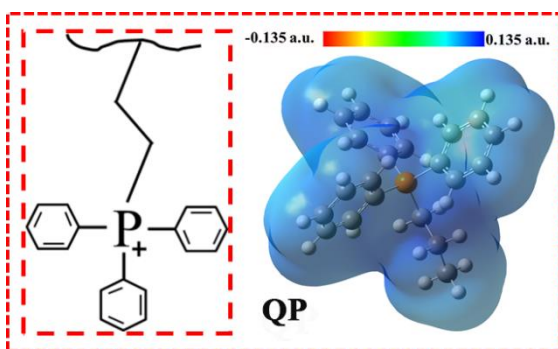
Fig. 3c and d presented the stress–strain curves of membranes for probing their strength and elasticity. CS was a semi-crystalline polymer which displayed acceptable mechanical stability with Young's modulus of 972.0 MPa, along with the tensile strength of 43.1 MPa and the elongation at break of 13.6%. In comparison, the composite membranes exhibited enhanced tensile strength values of 51.5 MPa and 44.7 MPa for CS/GO-1.5 and CS/QPGO-1.5, respectively. The increased tensile strength of composite membrane should originate from the superior rigidity of GO species. The mechanical properties of the membranes in this study were comparable to the membrane reported in the literature (Table 2). Compared with CS/GO, the entanglement between the CS chains and polymer brushes on QPGO, rather than the strong interfacial hydrogen bond interaction in CS/GO, endowed CS/QPGO with elevated elongation at break of 11.3% compared to CS/GO of 7.4%. Collectively, the incorporation of the GO species afforded composite membrane enhanced mechanical properties, with the Young's modulus reaching 1446.3 and 1058.3 MPa for CS/GO and CS/QPGO, respectively. Fig. 3d showed the mechanical stability of the membrane as a function of filler content. With the increase of filler content, composite membranes displayed decreased tensile strength and elongation at break.

### 3.3. Molecular Electrostatic Potential (MEP), IEC values, Water Uptake, and Swelling Ratio

The conduction ability and amount of functional groups along the transfer channels were important parameters for hydroxide conductivity of membranes. Various quaternary phosphonium (QP) groups had been applied to alkaline anion exchange membrane. To have a better understanding of the character of the QP group used in this study, the space structure, MEP, and molecular polarity of the QP were calculated in the GAUSSIAN 09W package at the DFT/B3LYP /6-311G(+d, +p) level, and the MEP maps were shown in Fig. 4a. The total charge of QP group was 0.135 a.u., which was much lower than those of QA groups in other studies (Fig. S1). The low electrostatic potential should result from the delocalization effect of benzene ring, which drove the electron cloud partially to P atom. Further evidence could be seen from the difference of electric potential between QP group with alkyl and benzene ring ligand as illustrated in Fig. S1. In addition, the faint interaction between QP and OH<sup>-</sup>

gives QP enhanced dissociation ability as well as the  $\text{OH}^-$  conduction capability (as the comparison between  $-\text{COOH}$  and  $-\text{SO}_3\text{H}$ ). The amount of conduction groups in the membranes was illustrated by *IEC* value, which was measured by titration method and the results were shown in Fig. 4b. GO displayed minimal *IEC* values due to the absence of conductive functional group. By comparison, QPGO exhibited a higher *IEC* value reaching  $2.05 \text{ mmol g}^{-1}$ , relative to pristine GO of  $0.05 \text{ mmol g}^{-1}$ . CS control membrane displayed an *IEC* value of  $0.40 \text{ mmol g}^{-1}$ , comparable with the value reported in literatures. [39,40,45] Compared with CS control membrane, CS/GO-1.5 displayed slightly decreased *IEC* value, due to the inferior *IEC* of GO, which diluted the concentration of available  $\text{OH}^-$  in composite membrane. In contrast, the high *IEC* of QPGO endowed QPGO-filled membranes with increased *IEC* values, giving a 3.75% enhancement of *IEC* to  $0.4156 \text{ mmol g}^{-1}$  for CS/QPGO-1.5%. The influence of QPGO content on *IEC* value of composite membrane was illustrated in Fig. 4b. The *IEC* values of the CS/QPGO-1.5 series increased as the filler content increase.

Water content in the membrane plays an important role in hydroxide ion conductivity since  $\text{H}_2\text{O}$  molecule can participate in the  $\text{OH}^-$  conduction through Grotthuss mechanism, diffusion, and convection mechanism. [46] Fig. 4c depicted the water uptake and swelling ratio of membranes at  $20^\circ\text{C}$ . The abundant hydroxyl and amino groups in the CS chains endowed the membrane with a high water absorbing capacity. CS control membrane attained a water uptake of 90%, close to the values in literature. [47] Incorporating GO or QPGO imparted composite membranes decreased water uptakes of 75.3 % and 84.5% for CS/GO-1.5 and CS/QPGO-1.5, respectively. This phenomenon should be ascribed to the increased tensile strength of composite membranes, which prohibited the swelling, as testified by the decreased swelling ratios of CS (32.5%) to 25.4% and 28.1% for CS/GO-1.5 and CS/QPGO-1.5, respectively. In addition, the lower water uptake of CS/GO-1.5 compared with CS/QPGO-1.5 should result from the strong interfacial interaction (hydrogen bond interaction) between GO and CS chains, which inhibited the swelling and thus water uptake. It was interesting to find that the water uptake and swelling ratio of CS/QPGO-*X* decreased with the increase of QPGO loading amount, regarding the tensile strength of CS/QPGO-*X* were inversely proportional to QPGO content. This phenomenon should be attributed to the relatively inferior hydrophilicity, which diluted the concentration of hydrophilic functional groups in composite membranes. In addition, all membranes exhibited elevated water uptakes and swelling ratios as temperature increased, due to the enhanced chain mobility, yet all the membranes maintained acceptable swelling ratios at  $80^\circ\text{C}$  (Fig. 4d).



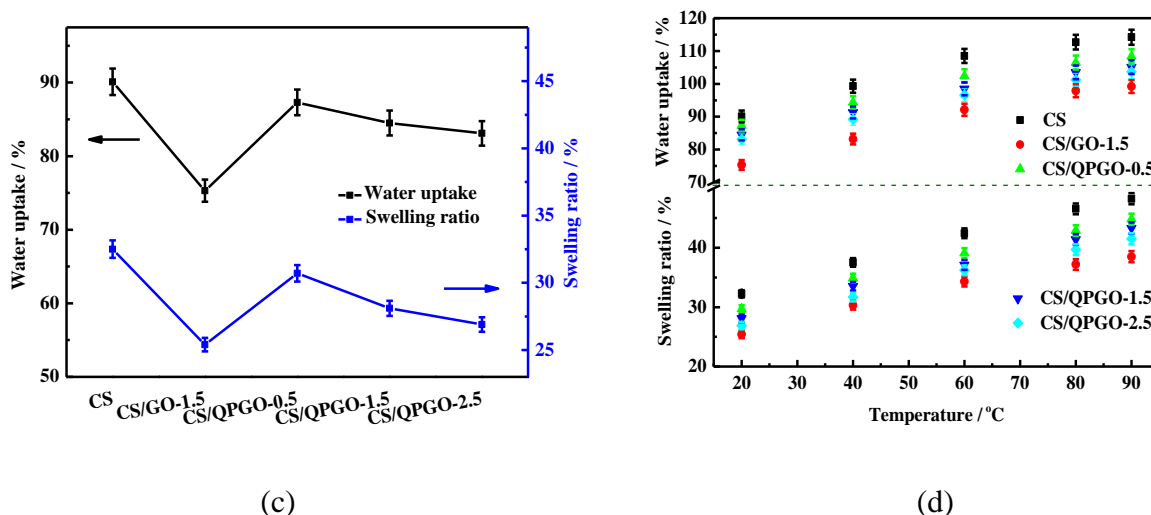


**Figure 4.** Molecular structure and the MEP the QP groups (a); *IEC* values of the materials and membranes (b); Water uptake and swelling ratio of the membranes at 20 °C (c); Temperature dependent water uptake and swelling ratio of the membranes (d).

### 3.4. Hydroxide Ion Conductivity

As the critical parameter of AEMs, hydroxide ion conductivity plays an important role in the fuel cell performance. For better investigating the  $\text{OH}^-$  conduction capability of composite membranes upon the incorporation of functionalized layer material, the conductivities under both saturated humidity (100% RH) and anhydrous conditions (0% RH) were measured, and the results were shown in Fig. 5a. CS control membrane attained an  $\text{OH}^-$  conductivity of  $1.46 \text{ mS cm}^{-1}$  at 20 °C under 100% RH. Incorporating GO conferred the composite membrane decreased hydroxide ion conductivity of  $0.78 \text{ mS cm}^{-1}$  due to the lower *IEC* and water uptake. In addition, CS/QPGO-1.5 with identical filler content attained an obviously enhanced hydroxide ion conductivity of  $4.66 \text{ mS cm}^{-1}$ , more than 220% augment compared to CS control membrane. The hydroxide ion conductivity enhancement was higher than other membranes reported in the literatures.[36,48,49] Considering that water uptake was an important parameter for  $\text{OH}^-$  conduction, since water could participate in  $\text{OH}^-$  conduction through several mechanisms (e.g., Grotthuss mechanism, diffusion, and migration), the reason for CS/QPGO-1.5 with lower water uptake and higher  $\text{OH}^-$  conduction ability should be stemmed from the presence of long-range transfer channels with locally enriched QP transfer sites along the interfaces, which paved low-energy-barrier pathways for efficient  $\text{OH}^-$  conduction. Similar phenomena could be seen in AEMs with micro-phase separation structures, where the membranes exhibited lower *IEC* and water uptake, yet displayed higher hydroxide ion conductivity than their disordered counterparts. Increasing the filler content resulted in the agglomeration of nanosheets and subsequent decrease of hydroxide ion conductivity (CS/QPGO-2.5). The positive contribution of the constructed interfacial transfer pathways of QPGO on  $\text{OH}^-$  conduction were further validated by testing membranes' anhydrous conductivity, where the influence of water on  $\text{OH}^-$  conduction was precluded. CS control membrane attained a hydroxide ion conductivity of  $2.56 \times 10^{-5} \text{ S cm}^{-1}$  at 20 °C under 0% RH. Incorporating GO afforded the composite membrane (CS/GO-1.5) a decreased hydroxide ion conductivity of  $1.69 \times 10^{-5} \text{ S}$

$\text{cm}^{-1}$ . In contrast, CS/QPGO-1.5 attained an enhanced hydroxide ion conductivity of  $4.95 \times 10^{-5} \text{ S cm}^{-1}$ , due to the presence of constructed long-range transfer channels with locally enriched transfer sites.

Temperature-dependent hydroxide conductivities of the obtained membranes under hydrated conditions were measured, and the results were shown in Fig. 5b. All the membranes exhibited hydroxide conductivity enhancements as testing temperature elevated, resulting from the promoted chain mobility and migration rate of  $\text{OH}^-$  at higher temperatures. [36,50] For instance, the conductivity of CS control membrane increased from 1.0 to 8.0  $\text{mS cm}^{-1}$  as the temperature elevated from 20 to 90 °C. CS/QPGO-X possessed higher conductivities than that of the CS control membrane at every temperature, and the maximum conductivity of 17.0  $\text{mS cm}^{-1}$  was obtained by CS/QPGO-1.5 at 90 °C. To gain further insight into the influence of the constructed low-energy-barrier pathway on  $\text{OH}^-$  conduction, the relationship between hydroxide conductivity and temperature were performed in Arrhenius plot. It could be seen that the experimental data was observed with an Arrhenius plot (Fig. 5c). The CS control membrane attained the  $E_a$  of 21.9  $\text{kJ mol}^{-1}$ , while the  $E_a$  values of CS/GO-1.5 increased to 22.3  $\text{kJ mol}^{-1}$  due to the absence of conductive sites on GO. By comparison, the  $E_a$  values of CS/QPGO-X decreased to the range of 19.7-18.5  $\text{kJ mol}^{-1}$ .

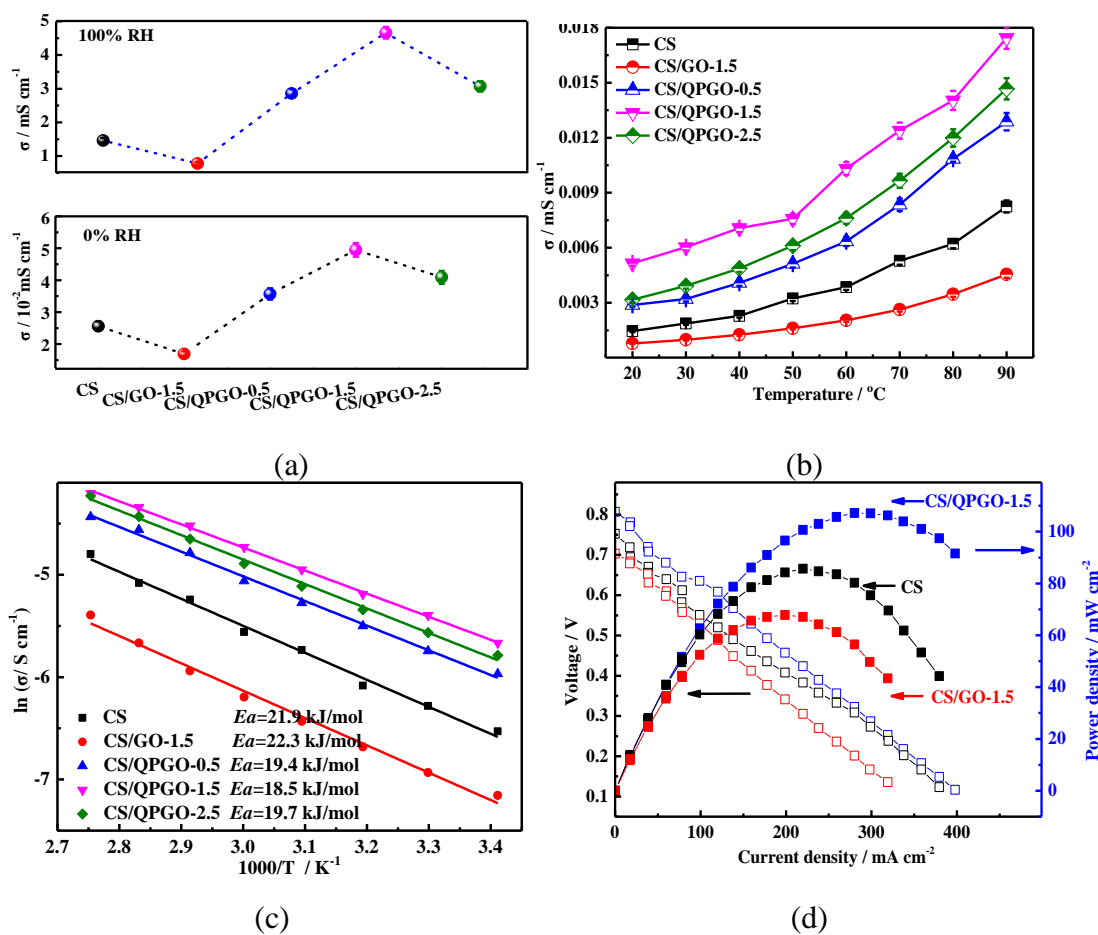


**Figure 5.** Hydroxide ion conductivities of the membranes at 20 °C under 0% and 100% RH (a); Temperature dependent conductivities of the membranes under 100% RH (b); Arrhenius plots of hydroxide conductivities of the membranes under 100% RH (c); Single-cell performances of the membranes in 4.0 M KOH + 5.0 M ethanol solution operated at 60 °C.

The decreased  $E_a$  was ascribed to the continuously distributed QP groups with highly conduction capability. Collectively, these results demonstrated that the constructed long-range transfer channels with locally enriched QP transfer sites were beneficial for efficient hydroxide conduction.

### 3.5. Fuel Cell Performance

CS control membrane, CS/GO-1.5, and CS/QPGO-1.5 were selected to better evaluate the fuel cell performances of as-prepared membranes. The fuel cells were assembled by using ethanol solution as fuel and oxygen as oxidizing agent (Fig. 5d). CS control membrane attained the OCV, maximum current density, and power density of 0.75 V, 379.4 mA cm<sup>-2</sup>, and 85.6 mW cm<sup>-2</sup>, respectively. By comparison, CS/GO-1.5 attained lower fuel cell performance due to the lower hydroxide ion conductivity. While, CS/QPGO-1.5 exhibited an obviously enhanced fuel cell performance, the OCV, maximum current density, and power density reached 0.80 V, 458.1 mA cm<sup>-2</sup>, and 110 mW cm<sup>-2</sup>, respectively. This enhancement should be mainly attributed to the lower transfer resistance for OH<sup>-</sup> conduction.

## 4. CONCLUSIONS

In conclusion, we attempted a facile method to enhance hydroxide ion conductivity of polymer membrane by incorporating quaternary phosphonium contained polymer brush functionalized graphene oxide. The brush-like structure imparted QPGO densely distributed and mobilized quaternary phosphonium groups. The selected quaternary phosphonium group was demonstrated with strong basicity and thus better OH<sup>-</sup> dissociation and conduction ability due to the delocalization effect of benzene ring. The generated polymer-filler interfaces served as long-range transfer channels with locally-enriched carrier sites for efficient OH<sup>-</sup> conduction. The unique structure afforded composite membranes higher *IEC* but lower water uptake and swelling ratio, associated with significantly enhanced hydroxide ion conductivity. Moreover, the composite membrane with QPGO exhibited higher fuel cell performance than CS control membrane and the maximum power density reached 110 mW cm<sup>-2</sup>. Collectively, architectures with deliberately designed long-range transfer channels and locally enriched carrier sites were beneficial for ion conduction, and incorporating polymer brush functionalized 1-D or 2-D materials was an efficient and facile method for the construction of this architecture in polymer.

## ACKNOWLEDGMENTS

We gratefully acknowledge the Key Scientific Research Project of Higher Education of Henan Province (No.17A430009), and the Science and Technology Planning Project of Henan (No.152102410072).

## ASSOCIATED CONTENT

## SUPPORTING INFORMATION

Molecular electrostatic potentials were calculated for quaternary ammonium as well as quaternary phosphonate with various ligands attached to the P atom, including  $-C_2H_5$ ,  $-C_4H_9$ , and a benzene ring. The molecular electrostatic potential was calculated in the GAUSSIAN 09W package at the DFT/B<sub>3</sub>LYP/6-311G (+d, +p) level.

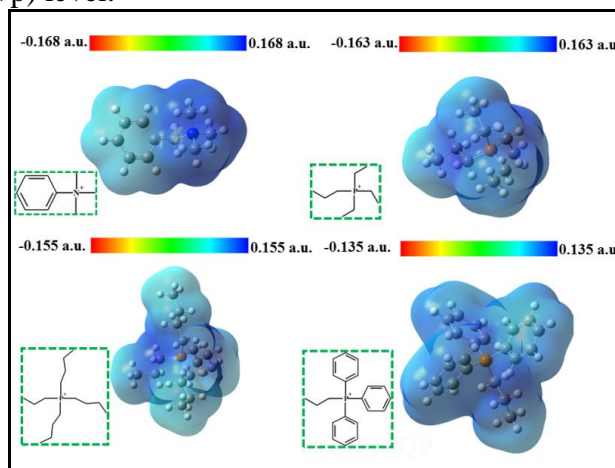


**Figure S1.** Molecular electrostatic potentials were calculated for quaternary ammonium as well as quaternary phosphonate with various ligands attached to the P atom, including  $-C_2H_5$ ,  $-C_4H_9$ , and a benzene ring. The molecular electrostatic potential were calculated in the GAUSSIAN 09W package at the DFT/B<sub>3</sub>LYP/6-311G (+d, +p) level.

## References

1. T. Feng, B. Lin, S. Zhang, N. Yuan, F. Chu, M. A. Hichner, C. Wang, L. J. Ding, *J. Membr. Sci.* 508 (2016) 7.
2. Y. Gao, F. Song, J. Qiao, S. Chen, X. Zhang, *J. Electrochim. Acta* 177 (2015) 201.
3. A.N. Lai, K. Zhou, Y.Z. Zhuo, Q.G. Zhang, A.M. Zhu, M.L. Ye, Q.L. Liu, *J. Membr. Sci.* 497 (2016) 99.
4. C. Lan, J. Fang, Y. Guan, H. Zhou, J. Zhao, *J. Power Sources* 295 (2015) 259.
5. K.H. Lee, D.H. Cho, Y.M. Kim, S.J. Moon, J.G. Seong, D.W. Shin, J.Y. Sohn, J.F. Kim, Y.M. Lee, *Energy Environ. Sci.* 10 (2017) 275.
6. J. Pan, C. Chen, Y. Li, L. Wang, L. Tan, G. Li, X. Tang, L. Xiao, J. Lu, L. Zhuang, *Energy Environ. Sci.* 7 (2014) 354.
7. J. Schauer, J. Hnát, L. Brožová, J. Žitka, K. Bouzek, *J. Membr. Sci.* 473 (2015) 267.
8. H. Wu, W. Jia, Y. J. Liu, *J. Mater. Sci.* 52 (2017) 1704.
9. Z. Si, Z. Sun, F. Gu, L. Qiu, F. Yan, *J. Mater. Chem. A* 2 (2014) 4413.
10. P. Papakonstantinou, V. Deimede, *RSC Adv.* 6 (2016) 114329.
11. S.D. Sajjad, D. Liu, Z. Wei, S. Sakri, Y. Shen, Y. Hong, F. Liu, *J. Power Sources* 300 (2015) 95.
12. Y. Wang, J. J. Qiao, R. Baker, J. Zhang, *Chem. Soc. Rev.* 42 (2013) 5768.
13. J.R. Varcoe, P. Atanassov, D.R. Dekel, A.M. Herring, M.A. Hickner, P.A. Kohi, A.R. Kucernak, W.E. Mustain, K. Nijmeijer, K. Scott, T. Xu, L. Zhuang, *Energy Environ. Sci.* 7 (2014) 3135.
14. Z. Zhang, K. Shen, L. Lin, J. Pang, *J. Membr. Sci.* 497 (2016) 318.
15. L. Zeng, T. S. Zhao, *J. Power Sources* 303 (2016) 354.

16. N. Yokota, M. Shimada, H. Ono, R. Akiyama, E. Nishino, K. Asazawa, J. Miyake, M. Watanabe, K. Miyatake, *Macromolecules* 47 (2014) 8238.
17. M. Tanaka, K. Fukasawa, E. Nishino, S. Yamaguchi, K. Yamada, H. Tanaka, B. Bae, K. Miyatake, M. Watanabe, *J. Am. Chem. Soc.* 133 (2011) 10646.
18. N.W. Li, Y.J. Leng, M.A. Hickner, C.Y. Wang, *J. Am. Chem. Soc.* 135 (2013) 10124.
19. Y. Xiong, Q.L. Liu, A.M. Zhu, S.M. Huang, Q.H. Zeng, *J. Power Sources* 186 (2009) 328.
20. E.D. Wang, T.S. Zhao, W.W. Yang, *Int. J. Hydrogen Energy* 35 (2010) 2183.
21. Q. Li, L. Liu, S. E. Liang, Q. B. Dong, B. K. Jin, R. K. Bai, *RSC Adv.* 3 (2013) 13477.
22. H. Bai, H. Zhang, Y. He, J. Liu, B. Zhang, J. Wang, *J. Membr. Sci.* 454 (2014) 220.
23. Y. Li, G. He, S. Wang, S. Yu, F. Pan, H. Wu, Z. Jiang, *J. Mater. Chem. A* 1 (2013) 10058.
24. J. Feng, H. Zang, Q. Yan, M. Li, X. Jiang, B. Cheng, *J. Appl. Polym. Sci.* 132 (2015) 41695.
25. T. Mu, Y. Cong, B. Zhang, *J. Appl. Polym. Sci.* 129 (2013) 3582.
26. B. M. Yoo, H. J. Shin, H. W. Yoon, H. B. Park, *J. Appl. Polym. Sci.* 396 (2014) 39628.
27. S. Das, A.S. Wajid, S.K. Bhattacharia, M.D. Wilting, I.V. Rivero, M.J. Green, *J. Appl. Polym. Sci.* 128 (2013) 4040.
28. S. Gu, R. Cai, Z. Chen, M. Sun, Y. Liu, G. He, Y. Yan, *Angew. Chem. Int. Ed.* 48 (2009) 6499.
29. D. Marcano, D. Kosynkin, J. Berlin, A. Sinitskii, Z. Sun, A. Slesarev, L. Alemany, W. Lu, J. Tour, *ACS Nano* 4(2010) 4806.
30. X. Liu, H. Cheng, Y. Liu, *Appl. Surf. Sci.* 280 (2013) 235.
31. Y. He, J. Wang, H. Zhang, T. Zhang, B. Zhang, S.K. Cao, J.D. Liu, *J. Mater. Chem. A* 2 (2014) 9548.
32. G. Zhao, T. Wen, X. Yang, S. Yang, J. Liao, J. Hu, D. Shao, X. Wang, *Dalton Trans.* 41 (2012) 6182.
33. P. Papakonstantinou, V. Deimede, *RSC Adv.* 6 (2016) 114329.
34. P. Kanti, K. Srigowri, J. Madhuri, B. Smitha, S. Sridhar, *Sep. Purif. Technol.* 40 (2004) 259.
35. R.J. Samuels, *J. Polym. Sci. Polym. Phys. Ed.* 19 (1981) 1081.
36. J.M. Yang, S.A. Wang, *J. Membr. Sci.* 477 (2015) 49.
37. Y. Wan, K.A.M. Creber, B. Peppley, V.T. Bui, *J. Appl. Polym. Sci.* 89 (2003) 306.
38. B. Lin, L. Qiu, J. Lu, F. Yan, *Chem. Mater.* 22 (2010) 6718.
39. X. Lin, L. Wu, Y. Liu, A.L. Ong, S.D. Poynton, J.R. Varcoe, T. Xu, *J. Power Sources* 217 (2012) 373.
40. C.C. Yang, S. Chiu, S. Kuo, T. Liou, *J. Power Sources* 199 (2012) 37.
41. W. Lu, Z. Shao, G. Zhang, Y. Zhao, J. Li, B. Yi, *Int. J. Hydrogen Energy* 38 (2013) 9285.
42. K. Hari Gopi, S. Gouse Peera, S.D. Bhat, P. Sridhar, S. Pitchumani, *Int. J. Hydrogen Energy* 39 (2014) 2659.
43. Q. Hu, Y. Shang, Y. Wang, M. Xu, S. Wang, X. Xie, Y. Liu, H. Zhang, J. Wang, Z. Mao, *Int. J. Hydrogen Energy* 37 (2013) 12659.
44. Y. Wu, C. Wu, J.R. Varcoe, S.D. Poynton, T. Xu, Y. Fu, *J. Power Sources* 195 (2010) 3069.
45. Y. Wan, B. Peppley, K.A.M. Creber, V.T. Bui, E. Halliop, *J. Power Sources* 162 (2006) 105.
46. G. Merle, M. Wessling, K. Nijmeijer, *J. Membr. Sci.* 377 (2011) 1.
47. M.W. Sabaa, N.A. Mohamed, R.R. Mohamed, N.M. Khalil, S.M. Abd El Latif, *Carbohydr. Polym.* 79 (2010) 998.
48. C.C. Yang, S.J. Chiu, W.C. Chien, S.S. Chiu, *J. Power Sources* , 195(2010) 2212.
49. Q. Li, L. Liu, S.E. Liang, Q.B. Dong, B.K. Jin, R.K. Bai, *RSC Adv.* 3(2013) 13477.
50. L. Zeng, T.S. Zhao, L. An, G. Zhao, X.H. Yan, *J. Membr. Sci.* 493 (2015) 340.